Aerothermodynamic Properties of an Upper Stage Rocket Equipped with Control Surfaces

Marília de Almeida Carvalho Matos
marilia.matos@tecnico.ulisboa.pt

Instituto Superior Técnico, Lisboa, Portugal

November 2019

Abstract

The most recent developments in the aerospace industry have made it clear that there is an emergent need to reuse every part of a launch vehicle. Although companies such as SpaceX, Blue Origin and Rocket Lab have already demonstrated their intentions to retrieve first stages, the controlled recovery of upper stages travelling at orbital speed is still a much more difficult task. This work aimed to study the reentry of an upper stage rocket equipped with control surfaces by using the CFD SPARK code, developed and maintained at Institute for Plasmas and Nuclear Fusion. The reentry velocity considered for the simulation was 7.6 km/s at an altitude of 60 km and two different geometries for the nose region thermal protection system were examined (one spherical and one highly elliptical). Aimed at determining the efficiency of the control surfaces and the most suitable thermal protection system, the aerodynamic coefficients and convective heat fluxes were computed, respectively, at that point of the trajectory for the two nose geometries, three flap deflection angles (10°, 20° and 30°) and four flap configurations. The two transport models considered (Wilke and Gupta-Yos/CCS) showed a good agreement within the shock-layer. Park's two-temperature model for thermal non-equilibrium was also analysed. The non-equilibrium state was particularly visible in the shock-wave region, whereas in the boundary layer, an almost perfect agreement exists between the two temperatures. The two geometries presented good aerodynamic similarity. The highest aerodynamic efficiency was found for the spherical nose geometry with a value of 0.19. The agreement between the results for the equilibrium and non-equilibrium cases supports the initial assumption of thermal equilibrium in the boundary layer.

Keywords: Reentry, Hypersonic CFD, SPARK, Aerothermodynamics, Control Surfaces, Heat Fluxes

1. Introduction

The control of a vehicle at lower speeds is achieved by making local alterations to the pressure field imparted on the vehicle by the flow. This can be accomplished with configurational changes, such as the deflection of a control surface. Hypersonic gas dynamics is fundamentally distinct from subsonic and supersonic ones, with the presence of strong high-temperature bow shocks, thermodynamic and chemical non-equilibrium where molecular vibrations, O_2 and N_2 dissociation, electronic excitation and ionisation take place. Therefore, the control and support of the distributed loads on the vehicle become much more difficult since, in addition to the pressure load, a distributed thermal load is being applied, mass flow (ablation) acts on the vehicle and additional shock waves can interact with the boundary layer and with the primary bow shock. [1]. Nevertheless, it is still necessary to guide the reentry vehicle so that it can navigate through the atmosphere with the right angles to withstand the friction and pressure occurring during atmospheric entry. Mastering and obtaining a complete knowledge of the physics of hypersonic flow is key for future space transportation missions, which include the return of soil samples originating in other celestial bodies and the safe transportation of space station experiments back to Earth. One way to achieve the aforementioned objectives is by using body flaps. These aerodynamic control surfaces can allow an entry vehicle to meet aerodynamic performance requirements while reducing or eliminating the use of ballast mass [2]. Furthermore, it provides the capability to modulate the lift-to-drag ratio during entry, to land the vehicle on a dedicated landing area as well as to satisfy other mission constraints, such as peak heat rate limits. The body flap guidance technology can also help the future development of reusable launcher stages, revealing its high importance in cost efficiency, since the recovery effort is almost eliminated.

The aerothermodynamic expertise needed to design and safely fly future hypersonic space vehicles is normally acquired by ground-based experimental simulation, computational predictions and ground-to-flight extrapolation methodologies. The best approach for improving confidence in aerothermodynamic design tools, both for the computational and for the ground-based experimental design tools, is to validate those tools and design approaches against flight experiments. Hence, the three main approaches to the study of the flow around a reentry vehicle are: ground-based experimental simulations, numerical simulations and flight experiments. Each one of these methods present intrinsic advantages and disadvantages. Different actively controlled reentry vehicles have been studied numerically and experimentally. Two emerging examples are the ESA flight experiment **EXPERT**, which promoted extensive aerothermodynamic simulations and wind tunnel tests in order to characterise the aerodynamic behaviour in the different regions of the atmosphere, ultimately leading to the compilation of an aerothermodynamic database [3] and the **Intermediate eXperimental Vehicle**, launched aboard a Vega rocket and returned to Earth subject to the same conditions as any other vehicle returning from low Earth orbit [4]. Its temperature and pressure sensors recorded information which is still being analysed in order to better understand the complexities of atmospheric reentry and help to design future reentry vehicles.

1.1. Case Study

In the near future, fully reusable rockets will be commonplace, suggesting a renewed emphasis on equipping upper stages to correctly perform the task of guided atmospheric reentry. The difficulty lies in the fact that these stages come back to Earth at a much higher speed than the first stage since they enter orbit on each mission in order to deploy satellites. This makes their return more challenging than recovering the first stage (a task currently being planned or performed by companies such as SpaceX, Blue Origin and Rocket Lab).

New focus has been given to small launch vehicles mainly due to the growth of CubeSat technology. These vehicles can place small satellites into low Earth orbits, starting from the ground or from an aerial platform. Hence, the geometry chosen to be aerodynamically characterised is the third stage of the European Vega launcher. This choice was based on the fact that its dimensions are within the dimensions of the upper stages of micro-launchers, the new trend in the aerospace field, and because it is the smallest among European launchers. Its stage 3/4 separation commonly takes place at a velocity between 7.5 and 7.8 $\mathrm{km\,s^{-1}}$ and at an altitude that does not exceed 215 km. The third stage consists of a Zefiro 9 engine, with its overall characteristics and performances presented in Fig. 1.

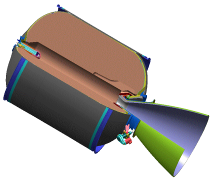

Zefiro 9	
Overall Length [m]	3.86
Diameter [m]	1.91
Propellant Mass [kg]	10115
Inert Mass [kg]	835
Nozzle Expansion Ratio	56
Nozzle Deflection Angle [°]	+/- 6

Figure 1: Z9 characteristics and performance [5].

This rocket engine is designed to work in vacuum conditions and thus, it cannot provide active control when entering the Earth's atmosphere.

1.1.1 Conceptual Design

Outfitting the third stage for a guided reentry and landing would result in a weight performance penalty since the extra mass would follow the mission payload all the way to orbit. This way, flexible thermal protection system (TPS) materials are a mission enabler for large mechanically inflatable or deployable reentry system aeroshells. An inflatable aeroshell provides one alternative for protecting the nose and nozzle sides of the vehicle with a low-mass design [6]. This concept applied to this case would result in the geometries represented in Fig. 2.

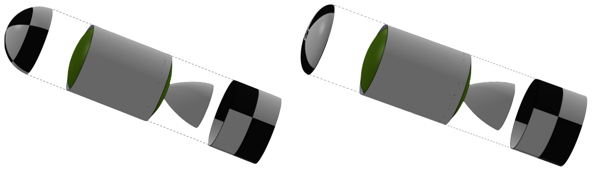

(a) Spherical nose (b) Highly elliptical nose

Figure 2: Stage equipped with parashield protection with two different nose geometries.

Two different nose geometries were considered in order to assess their influence on heat flux and flap efficiency: one spherical and one highly elliptical with an eccentricity of 0.9. Fig. 3 presents a possible flap configuration for the stage, using the same deployable mechanism. Although not represented in Fig. 3, all the simulations with the flap considered the nozzle protection system shown in Fig. 2.

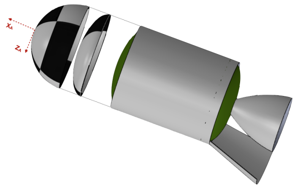

Figure 3: Stage equipped with control surface with two possible different nose geometries.

The overall aim of this work is to determine the aerodynamic characteristics of a reusable upper stage of a rocket from numerical results obtained with SPARK (the CFD code used to simulate multi-dimensional hypersonic flow, maintained at Instituto de Plasmas e Fusão Nuclear). In order to do so, the objectives are to: 1) identify a key trajectory point for the proper control set-up of the reentry body; 2) compute the convective heating experienced by the reentry vehicle at the selected key trajectory point; 3) assess the aerodynamic efficiency of control surfaces at orbital velocity reentry conditions; 4) generate aerodynamic and surface pressure data for future flight-test validation and aerodynamic database development.

2. Mathematical Formulation

To accurately model planetary entry conditions, it must be assumed that the number of collisions necessary to ensure chemical and thermal equilibrium in the chemically reacting gas has not had enough time to take place and therefore, the flow is said to be in a state of chemical and thermal non-equilibrium. In the special case of thermal equilibrium, all four energy modes (translational, rotational, vibrational and electronic excitation modes) share a single temperature, $T_k = T$.

A 9 species chemistry model is used to model weakly ionised air, consisting of the following chemical species: N_2, O_2, N, O, NO, NO^+, ${N_2}^+$, ${O_2}^+$, e^-. The two-temperature model for thermal non-equilibrium air flow proposed by Park [7] is also used in SPARK, as a compromise between the complex three temperature model and the over simplistic one temperature model. This model assumes two different temperatures: the translational-rotational global temperature $T_{\text{tra-rot}}$, common to the heavy species translational modes and rotational modes of the molecular species and the electron-vibrational-electronic temperature $T_{\text{vib-exc}}$, used to characterise the molecular vibrational, electron translational, and electronic excitation energies. Eqs. (1 - 4)) are the conservation equations applied to the conserved quantities of the flow (the basis to properly characterise the complex flow environment), under the assumption of continuum flow.

$$\frac{\partial(\rho c_i)}{\partial t} + \boldsymbol{\nabla}\cdot(\rho c_i \boldsymbol{U}) = -\boldsymbol{\nabla}\cdot\boldsymbol{J}_i + \dot{\omega}_i\,, \tag{1}$$

$$\frac{\partial(\rho \boldsymbol{U})}{\partial t} + \boldsymbol{\nabla}\cdot(\rho \boldsymbol{U}\otimes\boldsymbol{U}) = \boldsymbol{\nabla}\cdot[\tau] - \boldsymbol{\nabla}p + \boldsymbol{f}, \tag{2}$$

$$\frac{\partial(\rho E)}{\partial t} + \boldsymbol{\nabla}\cdot(\rho E\boldsymbol{U}) = -\boldsymbol{\nabla}\cdot\boldsymbol{q} - \boldsymbol{\nabla}\cdot(p\boldsymbol{U}) + \boldsymbol{\nabla}\cdot(\boldsymbol{U}\cdot[\boldsymbol{\tau}])\,, \tag{3}$$

$$\frac{\partial(\rho e_k)}{\partial t} + \boldsymbol{\nabla}\cdot(\rho\boldsymbol{U}h_k) = \boldsymbol{\nabla}\cdot\left(\kappa_k\boldsymbol{\nabla}T_k - \sum_i \boldsymbol{J}_i h_{i,k}\right) + \dot{\Omega}_k, \tag{4}$$

where ρ is the density, c_i is the i^{th} species mass fraction and $\boldsymbol{U}$ is the flow velocity vector. Considering a control volume in which a gradient in mass fraction of species i exists, J_i is the diffusion flux of species i, given approximately by Fick's Law as

$$\boldsymbol{J}_i \equiv \rho_i\boldsymbol{U}_i = -\rho\mathscr{D}_{im}\boldsymbol{\nabla}c_i\,, \tag{5}$$

where $\boldsymbol{U}_i$ is the velocity of species i and $\mathscr{D}_{im}$ is the multicomponent diffusion coefficient for species i through the mixture and is related to the binary diffusion coefficient $\mathscr{D}_{ij}$ through an expression based on the transport model being used. $\dot{\omega}_i$ is the species source term which takes into account the formation and destruction of each chemical species. p corresponds to the pressure and the viscous stress tensor $[\boldsymbol{\tau}]$ is given by

$$[\boldsymbol{\tau}] = \mu\left(\boldsymbol{\nabla}\boldsymbol{U} + (\boldsymbol{\nabla}\boldsymbol{U})^{\intercal}\right) - \frac{2}{3}\mu\left(\boldsymbol{\nabla}\cdot\boldsymbol{U}\right)[\mathbf{I}]\,, \tag{6}$$

where a Newtonian stress-strain rate relation for a fluid which obeys Stokes' hypothesis is used, μ is the gas viscosity and $[\mathbf{I}]$ is the identity matrix. $\boldsymbol{f}$ is the source term which represents the force density caused by any external force fields. $\boldsymbol{q}$ is the heat flux vector given by

$$\boldsymbol{q} = \sum_k \boldsymbol{q}_{C_k} + \sum_i \boldsymbol{J}_i h_i + \boldsymbol{q}_R, \tag{7}$$

h_i is the i^{th} species specific enthalpy and the total energy flux,

$$\boldsymbol{q}_E = -\sum_k \boldsymbol{q}_{C_k} - \sum_i \boldsymbol{J}_i h_i - \boldsymbol{q}_R - p\boldsymbol{U} + \boldsymbol{U}\cdot[\tau], \tag{8}$$

accounts for thermal conduction, transport of energy by diffusion, radiative energy emitted or absorbed by a fluid element element and rate of work done by pressure forces, shear stresses and normal stresses.

The Fourier's Law of heat conduction is used to compute the conduction heat flux vector for each thermal energy mode as

$$\boldsymbol{q}_{C_k} = -\kappa_k\boldsymbol{\nabla}T_k\,, \tag{9}$$

where κ_k and T_k are the thermal conductivity coefficient and temperature associated with the k^{th} energy mode, respectively. $\boldsymbol{q}_R$ is the radiative heat flux vector, considered equal to zero in this work and $\dot{Q}$ represents the source term. The additional conservation equation per non-equilibrium temperature needs to be considered (Equation 4) in order to accurately model non-equilibrium flow, where e_k is the global specific internal energy of the k^{th} thermal energy mode and $\dot{\Omega}_k$ is the source term associated with the k^{th} energy mode, out of the scope of this work.

2.1. Transport Models

Diffusion, viscosity and thermal conduction are the physical properties of transport phenomena which are important in high temperature viscous chemically reacting flows. Determining the flow transport coefficients is required to know the behaviour of the gas towards concentration, velocity and temperature gradients. SPARK is able to compute these properties using two different models based on mixing rules: the Wilke/Blottner/Eucken and the Gupta-Yos/CCS models. These simplified models substitute the computationally expensive Chapman-Enskog solution of the Boltzmann equation [8].

2.1.1 Wilke/Blottner/Eucken Model

This model was developed in 1950 with the application of kinetic theory to the full first-order Chapman-Enskog relation [9], along with curve fits for the species viscosities [10] and Eucken's relation [11] for the species thermal conductivities. Wilke assumed that all binary interactions have the same (hard-sphere) cross-section. This model gives a general equation for viscosity and thermal conductivity as a function of the properties of the pure components of the mixture [12]. This way, the mixture viscosity and thermal conductivity for each global temperature are given, respectively, by the following semi-empirical relations [10]:

$$\mu = \sum_i \frac{x_i \mu_i}{\phi_{ij}} \quad \text{and} \quad \kappa_k = \sum_i \frac{x_i \kappa_{k,i}}{\phi_{ij}}\,, \tag{10}$$

where x_i is the species mole fraction and ϕ_{ij} is the scale factor expressed as

$$\phi_{ij} = \sum_j x_j \left[1 + \sqrt{\tfrac{\mu_i}{\mu_j}} \left(\tfrac{M_j}{M_i}\right)^{\frac{1}{4}}\right]^2 \left[8\left(1 + \tfrac{M_i}{M_j}\right)\right]^{-\frac{1}{2}}\,, \tag{11}$$

where M_* representes each species' (i's or j's) molar mass. Blottner's curve fitting model [10] is then used to compute each species' viscosity and is given by

$$\mu_i(T_{\text{tra},i}) = 0.1 \exp(C_i)\; {T_{\text{tra},i}}^{(A_i \ln T_{\text{tra},i} + B_i)}\,, \tag{12}$$

where A_i, B_i and C_i are curve fitted coefficients for each species and $T_{\text{tra},i}$ is the translational temperature of species i.

Eucken's relation [11] can be used to determine the thermal conductivity of each species for each global thermal energy as

$$\begin{cases} \kappa_{k,i} = \frac{5}{2}\mu_i c_{v_{k,i}}, & \text{if } k = \text{tra} \\ \kappa_{k,i} = \mu_i c_{v_{k,i}}, & \text{if } k \neq \text{tra} \end{cases} \tag{13}$$

$c_{v_{k,i}}$ represents the specific heat at constant volume of the i^{th} species for the k^{th} energy mode. Depending on the multi-temperature model used, the contributions of each species should be accounted for differently in the mixing rule.

Finally, the diffusion coefficient is assumed equal to all species and is given by

$$\mathscr{D}_i = \mathscr{D} = \frac{\text{Le}\,\kappa}{\rho c_p}\,, \tag{14}$$

where c_p is the gas mixture total specific heat at a constant pressure, and the Lewis number Le, which corresponds to the ratio of thermal diffusivity to mass diffusivity, is assumed to be a constant.

2.1.2 Gupta-Yos/Collision Cross Section Model

The Gupta-Yos/CCS model is an approximate mixing rule which provides the transport properties, being also a simplification of the Chapman-Enskog solution [13]. This model takes into account the cross-section of each collision in the multicomponent mixture and thus accounts for the true nature of the interactions between species.

The collision terms are given by Eqs. 15 and 16, which define the strength of the interaction between each pair of species (i, j), as function of the controlling temperature T_c. This temperature depends on the type of particles colliding.

$$\Delta_{ij}^{(1)}(T_c) = \frac{8}{3}\left[\frac{2M_iM_j}{\pi R_u T_c (M_i + M_j)}\right]^{1/2} \pi\overline{\Omega}_{ij}^{(1,1)}\,, \tag{15}$$

$$\Delta_{ij}^{(2)}(T_c) = \frac{16}{5}\left[\frac{2M_iM_j}{\pi R_u T_c (M_i + M_j)}\right]^{1/2} \pi\overline{\Omega}_{ij}^{(2,2)}\,. \tag{16}$$

R_u is the universal gas constant and $\pi\overline{\Omega}_{ij}$ represents the average collision cross-section, computed using Gupta's curve fits [13].

The gas mixture viscosity μ is given by

$$\mu = \sum_i \frac{x_i m_i}{\sum\limits_j x_j \Delta_{ij}^{(2)}}\,, \tag{17}$$

where m_i is the particle mass of each species.

The translational mode κ_{tra} and electrons κ_{e} thermal conductivities are obtained as

$$\kappa_{\text{tra}} = \frac{15}{4} k_B \sum_{s \neq \text{e}} \frac{x_i}{\sum\limits_j \zeta_{ij} x_j \Delta_{ij}^{(2)}} \tag{18}$$

$$\text{and} \qquad \kappa_{\text{e}} = \frac{15}{4} k_B \frac{x_{\text{e}}}{\sum\limits_j \zeta_{\text{e}j} x_j \Delta_{ij}^{(2)}}\,, \tag{19}$$

where k_B is the Boltzmann constant and

$$\zeta_{ij} = 1 + \frac{[1 - M_i/M_j]\,[0.45 - 2.54(M_i/M_j)]}{[1 + (M_i/M_j)]^2}\,. \tag{20}$$

The thermal conductivities for the other modes of energy are computed as

$$\kappa_{\text{rot}} = \sum_{i=\text{mol.}} \frac{x_i m_i c_{v_{\text{rot},i}}}{\sum\limits_j x_j \Delta_{ij}^{(1)}}\,, \tag{21}$$

$$\kappa_{\text{vib}} = \sum_{i=\text{mol.}} \frac{x_i m_i c_{v_{\text{vib},i}}}{\sum\limits_j x_j \Delta_{ij}^{(1)}} \tag{22}$$

$$\text{and} \qquad \kappa_{\text{exc}} = \sum_{i \neq \text{e}} \frac{x_i m_i c_{v_{\text{exc},i}}}{\sum\limits_j x_j \Delta_{ij}^{(1)}}\,. \tag{23}$$

In the case of thermal equilibrium, the global thermal conductivity of the mixture κ is simply computed as the linear sum of Eqs. 18 through 23. Otherwise, the thermal conductivity associated with each global temperature mode k is obtained by taking the individual contributions of each species in the aforementioned equations, in agreement with the multi-temperature model used.

The binary diffusion coefficient involving two particles is given by

$$\mathscr{D}_{ij} = \frac{k_B T_c}{p\Delta_{ij}^{(1)}} \, . \tag{24}$$

An averaged diffusion coefficient can be used by assuming that the mixture is a binary mixture consisting of species i and all the remaining species in the mixture as one species j:

$$\mathscr{D}_i = \frac{1 - x_i}{\sum\limits_{j \neq i} \frac{x_j}{D_{ij}}} \, . \tag{25}$$

Both transport models are valid for weakly ionised flows. However, the latter is proved to be more physically accurate and numerically stable and faster in terms of convergence [9].

3. Numerical Setup

While in the vacuum of space, the upper stage rocket can orient itself using its movable nozzle adapted to vacuum conditions. When it reaches the upper layers of the atmosphere, its nozzle can no longer perform its job and the rocket stage needs to rely on its control surfaces to land on a dedicated area. The conditions at 60 km were chosen to be simulated since it is the maximum altitude that can be chosen which takes advantage of the continuum flow with no-slip boundary condition assumption, while having a free-stream pressure more than 20 times higher than, for example, at an altitude of 80 km. Moreover, heat loads are expected to be higher at 60 km than at any other point earlier in the trajectory. Also taking advantage of the ballistic geometry of the vehicle, the velocity attained while delivering its payload is very likely to be preserved at this altitude of the trajectory.

Table 1: Point simulation parameters.

h [km]	U_∞ [km s^{-1}]	p [Pa]	T [K]	ρ [kg m^{-3}]	Knudsen Nr.	M$_\infty$	x_{N_2}	x_{O_2}
60	7.60	21.96	247.00	3.096×10^{-4}	0.001	24	0.79	0.21

3.1. Mesh and Convergence Study

The boundary conditions for the CFD domain are the ones represented in Fig. 4, which include a fully catalytic and isothermal wall with its temperature set to $T_w = 1200$ K.

Varying the number of cells in the normal direction to the wall (Ni) is needed in order to assess which is the best configuration that allows to accurately capture the strong gradients experienced by the flow. Four different mesh resolutions were tested for the spherical nose geometry (60×200, 90×200, 105×200 and 150×200) with the same refinement near the wall and the results obtained for the temperature along the stagnation line are represented in Fig. 5. These results considered thermal equilibrium and the Gupta-Yos transport model.

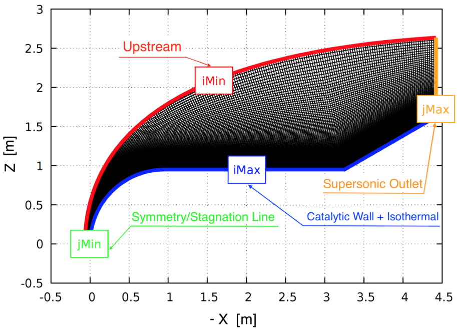

Figure 4: CFD boundary conditions for a 150x200 mesh configuration.

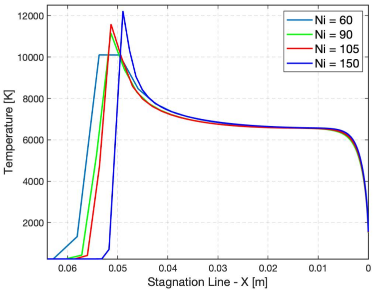

Figure 5: Temperature along the stagnation line for different number of cells normal to the wall.

Fig. 5 shows that the mesh with Ni = 60 is too rough to be considered in further simulations. Although predicting the conditions at the shock front is not as important as accurately predicting the boundary-layer conditions, this mesh configuration does not show a temperature peak associated to the shock region. Moreover, the lowest temperature achieved behind the shock front is 12% higher when compared to the 150×200 mesh configuration. The mesh configurations with Ni = 90 and 105 cells, also when compared to the 150×200 mesh, seem to underestimate the same temperature in 3.1% and 2.0%, respectively, the shock position up to 2.4×10^{-3} m, and the temperature peak up to 8.4%.

Taking all these factors into account, the mesh that is accepted to accurately predict the pressure, temperature profiles and, consequently, the heat flux and forces at the surface of the vehicle is the one with Ni = 150 cells.

The same study was performed for the highly elliptical nose geometry using four different mesh configurations (100×175, 120×175, 160×175 and 195×175), yielding Ni = 195 cells. The shock front moved 0.0513 m along the stagnation line when compared to the spherical geometry, which translates to a thicker shock layer, resulting in the need for a greater number of cells.

4. Results

4.1. Thermal Equilibrium

4.1.1 Impact of Transport Model

Figs. 6 (a) and (b) illustrate the stagnation line temperature profile and wall heat flux for the two mixing rules used in this work and for the spherical geometry. All reported heating results are convective only, which consists of a conduction and a diffusive component, determined by the temperature and mass fraction gradients, respectively. The contribution from radiation was not expected to be dominant, as in the case of objects travelling at super-orbital speeds (in which radiative heating mostly depends on the excited species) and was therefore excluded from the analysis.

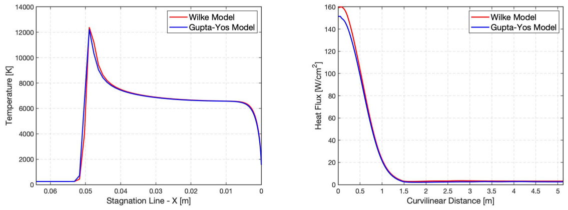

(a) Stagnation line temperature

(b) Wall heat flux

Figure 6: Temperature along the stagnation line and wall heat flux for the Wilke and Gupta-Yos transport models.

A thorough analysis of the results shows how the two models agree well at the velocity considered in this work. The greatest discrepancy is found at the bow shock region, which is already expected due to the roughness of this area. The Wilke model estimates the peak temperature to be 1.4% higher when compared to the Gupta-Yos model. Moreover, the lowest temperature achieved behind the shock is 1.5% higher in the Wilke case. Consequently, the heat flux in the nose region is 5.1% lower for the Gupta-Yos model, resulting in an almost perfect agreement after this region. The slight disturbances found in the nose area also suggest that the carbuncle problem was not completely eradicated even though several measures were applied [14] [15]. Moreover, the heat flux at the stagnation point for both models yields higher results than the semi-empirical Sutton-Graves relation[1] [16], which predicts a stagnation heat flux of 138 W cm^{-2}. This is expected since this relation assumes chemical equilibrium.

Fig. 7 shows that the pressure at the stagnation point for the Wilke model is slightly higher (0.23%) when compared to the Gupta mixing rule.

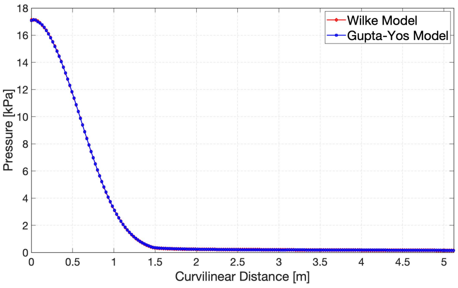

Figure 7: Wall pressure distribution, $\eta = 0°$.

The Gupta-Yos/CCS model is assumed to be more physically accurate given that this mixing rule takes into account the cross-section of each collision in the multi-component mixture and thus accounts for the true nature of the collisions between species. Hereupon the results are based on the Gupta-Yos/CCS model and a fully catalytic boundary condition at the wall is considered.

4.2. Stagnation Line Analysis

Fig. 8 presents the results for the species mole fractions along the stagnation line, thus showing how x_i varies behind the shock front.

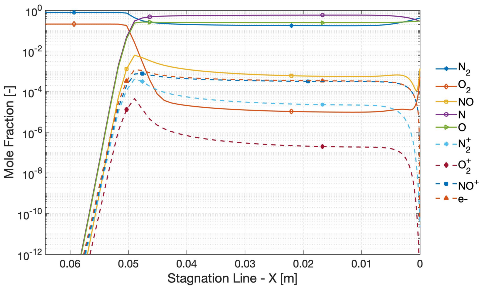

Figure 8: Species mole fractions in thermal equilibrium.

The N$_2$ and O$_2$ mole fractions remain constant ($x_{N_2} = 0.79$ and $x_{O_2} = 0.21$), until the bow shock is reached. From this point on (X = 0.053 m), given the temperatures in excess of 9000K attained in the shock region, dissociation and ionisation of the molecules take place. N$_2$ and O$_2$ species mole fractions decrease and the rest of the species (atomic, ionic and electrons) mole fractions increase. The number of electrons increases rapidly downstream from the shock-wave and its mole fraction reaches a maximum value of 0.0012 and then diminishes quickly toward the vehicle surface. The chemical composition of the gas slightly stabilises before the boundary layer is reached, where, once again, temperature gradients promote chemical reactions of the species that constitute the gas. x_{N_2}, x_{O_2} and x_{NO} rapidly increase at the surface, while $x_{N_2^+}$, $x_{O_2^+}$ and x_{NO^+} decrease, suggesting that the latter are recombining with e$^-$ to form the former species.

---

[1] $q = K\sqrt{\frac{\rho}{R_n}}U^3$, where K is the heat transfer coefficient and R_n is the nose radius.

4.2.1 Impact of Nose Geometry

Fig. 9 shows the temperature along the stagnation line, and the wall heat flux profile for both geometries considered in this work.

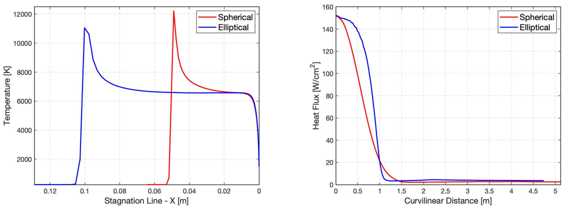

(a) Stagnation line temperature (b) Wall heat flux

Figure 9: Temperature and heat flux profiles for the two different nose geometries.

Fig. 9 (a) illustrates that the shock layer is thicker for the elliptical nose geometry, with a wider shock front being 0.0513 m further away from the vehicle surface when compared to the spherical case. Although the latter shows a higher temperature peak, no significant conclusions can be withdrawn regarding the shock front due to the roughness of the area. The heat flux at the stagnation point differs less than 0.5% and the wall heat flux profile differs in shape with a plateau value of 2.6 and 3.6 $\mathrm{W\,cm^{-2}}$ for the spherical and elliptical cases, respectively.

The pressure peak at the stagnation point was found to be 0.3% higher in the elliptical case when compared to the spherical one.

4.3. Thermal Non-Equilibrium

Fig. 10 illustrates the impact of considering Park's two-temperature model to account for thermal non-equilibrium on the temperature and pressure profiles along the stagnation line for the spherical nose geometry. For comparison purposes, the equilibrium results are reported in dashed lines.

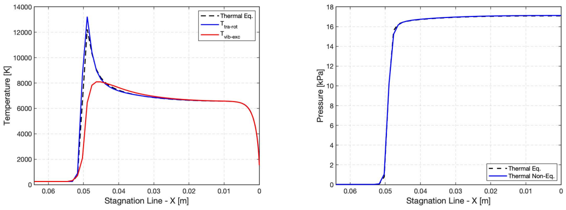

(a) Stagnation line temperature (b) Stagnation line pressure

Figure 10: Temperature and pressure profiles along the stagnation line for both thermal equilibrium and non-equilibrium.

As can be seen in Fig. 10 (a), the peak in translational-rotational temperature (blue line) is 8.2% higher for the non-equilibrium case, with the same overall trend as the equilibrium case. Moreover, the non-equilibrium case reveals a wider shock front and an increase in the shock standoff distance. The electron-vibrational-electronic temperature peak (red line) is 38.8% lower than that of the translational-rotational temperature and follows a very distinct profile up until X = 0.013 m. This leads to the conclusion that the flow is in a state of very strong non-equilibrium in the shock layer, reaching thermal equilibrium in the boundary layer region.

The pressure in thermal non-equilibrium is assumed to be the sum of the heavy species pressure and the free electrons' pressure, which are functions of the translational and the free electrons' temperature, respectively. Expectedly, since the pressure is not affected by the internal degrees of freedom of the particles, the pressure profile for both equilibrium and non-equilibrium conditions is the same within the shock layer, as illustrated in Fig. 10 (b). Moreover, apart from the wider shock front, the stagnation line flow composition does not change significantly with respect to the thermal equilibrium case and the heat flux results at the stagnation point showed a difference smaller than 10% between the two cases.

The small differences encountered in this analysis allows to assume thermal equilibrium combined with chemical non-equilibrium in further simulations.

4.4. Impact of Flap Deflection Angle

Fig. 11 shows how the temperature changes along the stagnation line and the wall heat flux for the different flap deflection angles η, considering the circular nose geometry. As expected, the stagnation line profile only changes slightly, with stagnation point temperatures not varying when compared to the zero deflection angle case (black dashed line). Since the flow is supersonic behind the shock front, the deflection of a control surface does not affect the heat flux in the nose region.

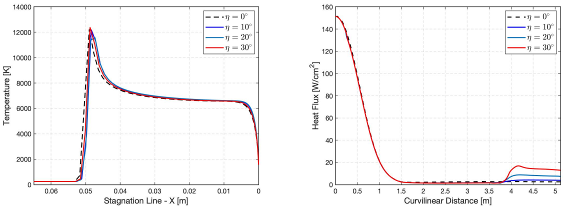

(a) Stagnation line temperature (b) Wall heat flux

Figure 11: Temperature profile along the stagnation line and wall heat flux for different flap deflection angles.

Regarding the wall heat flux (Fig. 11 (b)), for the $\eta = 10°$ and $\eta = 20°$ cases, the heat flux at the stagnation point is found to be slightly higher with respect to the baseline case ($\eta = 0°$). However, there is no reason to believe that the flap deflection angle has a direct or significant influence on the stagnation point heat flux, since the same trend is not observed in the $\eta = 30°$ case. Naturally, the flap deflection introduces a new shock-wave within the flow at a curvilinear distance around 3.75 m, which increases the temperature behind it. Consequently, this leads to an increase in the heat flux and its magnitude increases as the flap deflection angle increases. The peak in heat flux for this region and for the $\eta = 30°$ case is 558% higher than for the baseline case, while for the $\eta = 10°$, this scenario corresponds to a 62.7% increase in heat flux.

The wall pressure distribution for the different angle deflections is also plotted in Fig. 12. From the stagnation point on up until the flap region, the pressure profile remains the same for all the cases. As the flap is reached by the flow, a shock-wave is, once again, responsible for increasing the pressure behind it. These effects change the forces and moments acting on the vehicle.

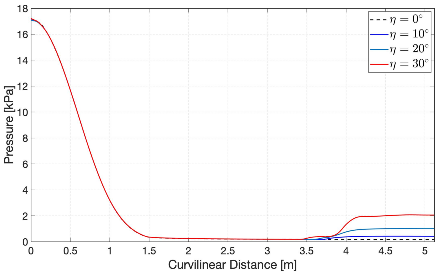

Figure 12: Wall pressure distribution.

A slight disturbance of the pressure is observed around a curvilinear distance of 3.5 m for the $\eta = 20°$ and $\eta = 30°$ cases, with the latter having the most visible effect. This disturbances are caused by the subsonic portion of the boundary layer on the vehicle's surface approaching the compression ramp which provides a path for the disturbances such as the increased pressure produced by the shock wave to influence the upstream flow. Negative values for the velocity were found in the control surface region, supporting the premise of flow separation.

Similar conclusions can be withdrawn for the elliptical geometry.

4.5. Aerodynamic Coefficients

Two algorithms were generated in order to compute the forces and moments acting on the reentry vehicle. The first one considers the normal (pressure) forces and was validated considering some cases to which the results were already known. In flows at speeds greater than the speed of sound, a perturbation is only felt in the Mach cone (Mach angle given as a function of Mach number M as $\arcsin(\mathrm{M}^{-1})$) downstream from the source of disturbance, and therefore, certain parts of the flap behave as though they were in the two-dimensional flow. Taken this into account, a correction factor was introduced in the pressure distribution along the flap in order to include the three-dimensional flow effects on the control surface [17] . This correction factor is represented in Fig. 13 (not to scale).

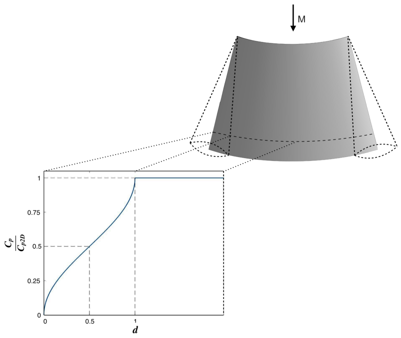

Figure 13: Symmetric pressure profile along the flap taken into account 3D effects (not to scale).

The pressure correction in the mach cone region is given by

$$\Delta p = \Delta p_{2D} \frac{2}{\pi} \arcsin \sqrt{d}. \tag{26}$$

The pressure profile remains the same as in the simulations until the disturbed region, which is under the influence of the side edges, is reached. d is a dimensionless number that quantifies the distance along the perturbed region of the trailing edge of the flap.

The second algorithm takes into account the tangential (shear) forces.

The forces and aerodynamic coefficients were calculated for a reference area of 2.84 m^2 for both geometries and for a reference chord of 4.6 and 4.06 m for the spherical and elliptical geometry, respectively. Three different flap angles were used ($\eta = 10°, 20°$ and $30°$) and four different flap configurations considered.

180° Flap Configuration Centred at $\mathbf{Y}_A = \mathbf{0}$ m and $\mathbf{Z}_A = \mathbf{0.95}$ m: Fig. 14 shows the 180° flap concept centred at $\mathrm{Y}_A = 0$ m and $\mathrm{Z}_A = 0.95$ m.

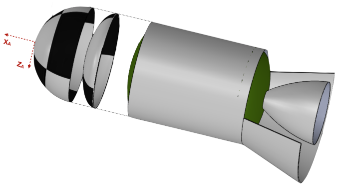

Figure 14: Rocket's stage equipped with a 180° flap centred at $\mathrm{Y}_A = 0$ m and $\mathrm{Z}_A = 0.95$ m.

The results obtained for the drag, lift and moment coefficients are represented in Figs. 15 and 16. Apart from the drag coefficient, the resulting forces and moments for both nose geometries and both equilibrium and non-equilibrium (2T in dashed line) are very similar. The maximum discrepancy is found with a flap deflection angle of $\eta = 30°$ in the moment coefficient about mid-chord and corresponds to a 3.14% negative increase in C_{MY_A} for the spherical geometry when compared to the elliptical one. With respect to the spherical geometry, the highly elliptical nose shows a drag coefficient (Fig. 15 (a)) up to 52% higher ($\eta = 0°$ case). Between the equilibrium and non-equilibrium case for the circular geometry, the differences are not higher than 3% for any deflection angle. The maximum aerodynamic efficiency (L/D) is 0.19 obtained when the flap is deflected with an angle of 30° for the circular geometry.

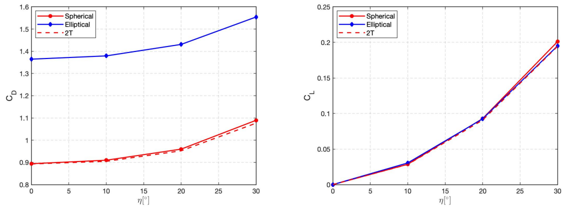

(a) Drag coefficient (b) Lift coefficient

Figure 15: Drag and lift coefficients.

Naturally, since the flap is symmetric with respect to the plane defined by $\mathrm{Y}_A = 0$ and centred at $\mathrm{Z}_A = 0.95$ m, the only moment about $\{\mathrm{X}_A, \mathrm{Y}_A, \mathrm{Z}_A\} = \{0, 0, 0\}$ m is the moment with respect to the Y_A axis (Fig. 16: pitching moment).

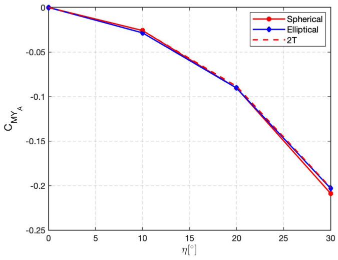

Figure 16: Pitching moment coefficient about $\{\mathrm{X}_A, \mathrm{Y}_A, \mathrm{Z}_A\} = \{0, 0, 0\}$ m

90° Flap Configuration Centred at $\mathbf{Y}_A = 0$ m and $\mathbf{Z}_A = 0.95$ m: The 90° flap concept centred at $\mathrm{Y}_A = 0$ m is the one represented in Fig. 3. This new symmetric flap configuration presents different results for all the coefficients when compared to the previous configuration, except for the $\eta = 0°$ case. The maximum drag and lift coefficients in equilibrium conditions are 6.5% and 34.5% higher, respectively, when compared to the 180° flap configuration. The maximum aerodynamic efficiency is 0.13, 31% lower than for the first configuration. The maximum negative value obtained for the moment coefficients with respect to the Y_A axis is 0.13 for the reference point at the origin.

90° Flap Configuration Centred at $\mathbf{Y}_A = 0.67$ m and $\mathbf{Z}_A = 0.67$ m: Fig. 17 shows the 90° flap concept centred at $\mathrm{Y}_A = 0.67$ m and $\mathrm{Z}_A = 0.67$ m. This flap is not symmetric with respect to the plane defined by $\mathrm{Y}_A = 0$ and therefore, additional moments are created by the aerodynamic forces around the Z_A axis (yawing moment).

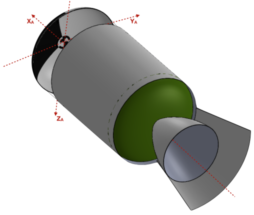

Figure 17: Rocket's stage equipped with a 90° flap centred at $\mathrm{Y}_A = 0.67$ m and $\mathrm{Z}_A = 0.67$ m

.

According to the results of Fig. 18, the aerodynamic efficiency is not higher than 0.094 for the deflection angles considered. The moment coefficient with respect to the Y_A axis is -0.1 for the maximum flap deflection angle considered. The results for the moment coefficients with respect to the Z_A axis about $\{\mathrm{X}_A, \mathrm{Y}_A, \mathrm{Z}_A\} = \{0, 0, 0\}$ m are symmetric to the ones shown in Fig. 19.

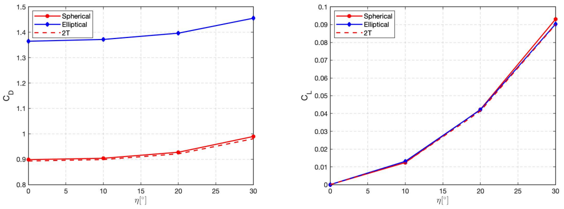

(a) Drag coefficient (b) Lift coefficient

Figure 18: Drag and lift coefficients.

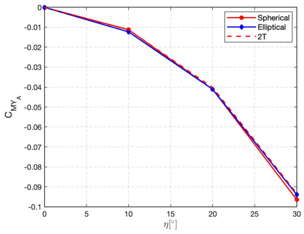

Figure 19: Pitching moment coefficient about $\{\mathrm{X}_A, \mathrm{Y}_A, \mathrm{Z}_A\} = \{0, 0, 0\}$ m

Additionally, a 45° flap configuration centred at $\mathrm{Y}_A = 0.36$ m and $\mathrm{Z}_A = 0.88$ m was considered. This configuration leads to the lowest aerodynamic efficiency of all the flap configurations studied when the maximum deflection angle is considered, with a value of 0.062, for the circular case. Although this configuration represents only half the mass of the previous one, it also represents a significant decrease in efficiency in terms of moments and forces.

5. Conclusions

The influence of the transport model, nose geometry, multi-temperature model and flap angle and configuration on the reentry of a rocket's upper stage equipped with control surfaces was successfully analysed. The development of a post-processing algorithm allowed to compute the aerodynamic forces and moments acting on the vehicle.

The analysis of the transport model concluded that the Wilke model slightly overestimates the temperature profile when compared to the Gupta-Yos model and thus, the heat flux at the stagnation point is lower for the latter. In terms of the pressure profile, no significant differences were found.

The main difference found between the two nose geometries was the increase of 0.0513 m in the thickness of the shock layer for the elliptical case.

Non-equilibrium simulations revealed a strong non-equilibrium in the shock-wave region. Nonetheless, thermal equilibrium was reached in the boundary layer, which allowed to use the more time-efficient equilibrium model in further simulations. Within the shock layer, the pressure profiles for both states were found to be the same, since the pressure is not affected by the internal degrees of freedom of the particles.

At last, the aerodynamic coefficients were obtained for four different flap configurations and three positive deflection angles. The maximum aerodynamic efficiency was found for the spherical geometry ($L/D = 0.19$). Additional 2T temperature simulations proved that this assumption does not significantly alter the results.

The future steps recommended for this work are: 1) CFD simulations in further points of the trajectory with the estimated aerodynamic coefficients as inputs for the trajectory code; 2) true multidimensional analysis, including gaps and other interfaces; 3) turbulence analysis in the region away from the stagnation point; 4) thermal protection system design, including the selection of the effective and lightweight materials able to withstand the heating loads generated during the trajectory and 4) assessment of the recovery system's potential impact on the launcher's lifting capability.

References

[1] F. J. Regan and S. M. Anandakrishnan, *Dynamics of Atmospheric Re-Entry.* AIAA, 1993.

[2] A. Korzun, K. J. Murphy, and K. Edquist, "Supersonic aerodynamic characteristics of blunt body trim tab configurations," in *31st AIAA Applied Aerodynamics Conference*, AIAA 2013-2809, June 2013.

[3] M. Di Clemente, M. Marini, S. "Di" Benedetto, A. Schettino, and G. Ranuzzi, "Numerical prediction of aerothermodynamic effects on a reentry vehicle body flap configuration," *Acta Astronautica*, vol. 65, pp. 221–239, 2009.

[4] P. Baiocco, S. Guedron, S. Plotard, and J. Moulin, "The pre-X atmospheric re-entry experimental lifting body: Program status and system synthesis," In *57th International Astronautical Congress.* Paper 06-D2.P.2.02, 2006.

[5] S. Bianchi, "The Launchers and the Vega Programme and the Launcher Subsystems." Directorate of Launchers, ESA, February 2005.

[6] R. Savino and V. Carandente, "Aerothermodynamic and feasibility study of a deployable aerobraking re-entry capsule," *Fluid Dynamics & Material Processing*, vol. 8, pp. 453–477, December 2012.

[7] C. Park, "Assessment of two-temperature kinetic model for ionizing air," *Journal of Thermophysics and Heat Transfer*, vol. 3, pp. 233–244, July 1989.

[8] S. Chapman and T. G. Cowling, *The Mathematical Theory of Non-uniform Gases.* Cambridge Mathematical Library, 3rd ed., 1970.

[9] G. E. Palmer and M. J. Wright, "A comparison of methods to compute high-temperature gas viscosity," *Journal of Thermophysics and Heat Transfer*, vol. 17, April 2003.

[10] F. G. Blottner, M. Johnson, and M. Ellis, "Chemically reacting viscous flow program for multi-component gas mixtures," Technical Report SC-RR-70-754, January 1971.

[11] G. Palmer and M. Wright, "A comparison of methods to compute high-temperature gas thermal conductivity," In *36th AIAA Thermophysics Conference*, 2003.

[12] C. R. Wilke, "A viscosity equation for gas mixtures," *The Journal of Chemical Physics*, vol. 18, 1950.

[13] R. N. Gupta, J. M. Yos, R. A. Thompson, and K.-P. Lee, "A review of reaction rates and thermodynamic and transport properties for an 11-species air model for chemical and thermal non-equilibrium calculations to 30000 K." Technical Report NASA-RP-1232, 2002.

[14] R. W. MacCormack, "Carbuncle computational fluid dynamics problem for blunt-body flows," *Journal of Aerospace Information Systems*, vol. 10, May 2013.

[15] M. Pandolfi and D. D'Ambrosio, "Numerical instabilities in upwind methods: Analysis and cures for the carbuncle phenomenon," *Journal of Computational Physics*, vol. 166, 2001.

[16] K. Sutton and R. A. Graves, "A general stagnation-point convective heating equation for arbitrary gas mixtures," Technical Report NASA-TR-R-376, November 1971.

[17] J. C. F. Pereira, *Aerodinâmica Compressível.* AEIST, 2018. Sebenta de Aerodinâmica II.